16 nm-resolution lithography using ultra-small-gap bowtie apertures

You may also be interested in:

Calibration of exposure dose for nanoscale plasmonic lithography with microsized far-field spot patterns
Dandan Han, Changhoon Park, Howon Jung et al.

Plasmonic lithography for fabricating nanoimprint masters with multi-scale patterns
Howon Jung, Seok Kim, Dandan Han et al.

Engineering metallic nanostructures for plasmonics and nanophotonics
Nathan C Lindquist, Prashant Nagpal, Kevin M McPeak et al.

Contact-pressure reduction of pyramidal optical probe array on corrugated aluminium/silicon nitride membranes
Jinhee Jang, Seonghyeon Oh and Jae W Hahn

Fabrication of a plasmonic modulator incorporating an overlaid grating coupler
Sa'ad Hassan, Ewa Lisicka-Skrzek, Anthony Olivieri et al.

Application of Solid Immersion Lens-Based Near-Field Recording Technology to High-Speed Plasmonic Nanolithography
Kyoung-Su Park, Taeseob Kim, Won-Sup Lee et al.

Hybrid strategies in nanolithography
Héctor M Saavedra, Thomas J Mullen, Pengpeng Zhang et al.

Fabrication and modelling of fractal, biomimetic, micro and nano-topographical surfaces
Daniel J T Kyle, Antonios Oikonomou, Ernie Hill et al.

16 nm-resolution lithography using ultra-small-gap bowtie apertures

Yang Chen[1,4], Jin Qin[2,4], Jianfeng Chen[1], Liang Zhang[2], Chengfu Ma[1], Jiaru Chu[1,5], Xianfan Xu[3,5] and Liang Wang[2,5]

[1] Micro and Nano Engineering Lab, University of Science and Technology of China, Hefei City, Anhui Province 230026, People's Republic of China
[2] Department of Optics and Optical Engineering, Anhui Key Laboratory of Optoelectronic Science and Technology, University of Science and Technology of China, Hefei City, Anhui Province 230026, People's Republic of China
[3] School of Mechanical Engineering and Birck Nanotechnology Center, Purdue University, West Lafayette, IN 47907, United States

E-mail: jrchu@ustc.edu.cn, xxu@ecn.purdue.edu and lwang121@ustc.edu.cn

CrossMark

Abstract

Photolithography has long been a critical technology for nanoscale manufacturing, especially in the semiconductor industry. However, the diffractive nature of light has limited the continuous advance of optical lithography resolution. To overcome this obstacle, near-field scanning optical lithography (NSOL) is an alternative low-cost technique, whose resolution is determined by the near-field localization that can be achieved. Here, we apply the newly-developed backside milling method to fabricate bowtie apertures with a sub-15 nm gap, which can substantially improve the resolution of NSOL. A highly confined electric near field is produced by localized surface plasmon excitation and nanofocusing of the closely-tapered gap. We show contact lithography results with a record 16 nm resolution (FWHM). This photolithography scheme promises potential applications in data storage, high-speed computation, energy harvesting, and other nanotechnology areas.

Keywords: near-field lithography, nanofabrication, localized surface plasmon, nanofocusing, passive flexure stage

(Some figures may appear in colour only in the online journal)

1. Introduction

In the past decades, photolithography has achieved great success and has pushed forward the development of nanotechnology [1]. Its further advance is restricted by the diffractive nature of light. To economically realize high-resolution and high-throughput optical nano-patterning, various lithography techniques have been developed, such as self-assembly lithography, nano-sphere lithography, plasmonic interference lithography and nanoimprint lithography [2–6]. Among them, near-field scanning optical lithography (NSOL) using ridged apertures has attracted intensive attention [7–10]. In NSOL, scanning nano-apertures serve as diffraction-unlimited light sources and directly expose surface features in the optical near field on the photoresist; nano-apertures with a more confined near field are therefore preferred to achieve better lithography resolution. For a bowtie aperture illuminated with proper polarization, its near-field localization is decided by its gap size [11, 12].

Usually, nanoscale bowtie apertures are directly milled using a focused ion beam (FIB) from the top of a thin metal film; we call it 'the front-side milling method'. However, bowtie apertures fabricated by this method suffer from a tapered sidewall with a rounded corner [13]. The tapered sidewall is caused by the combined effects of the Gaussian ion beam profile, the angle-dependent sputtering yield of the incident ion, and redeposition. The rounded corner is mainly

---
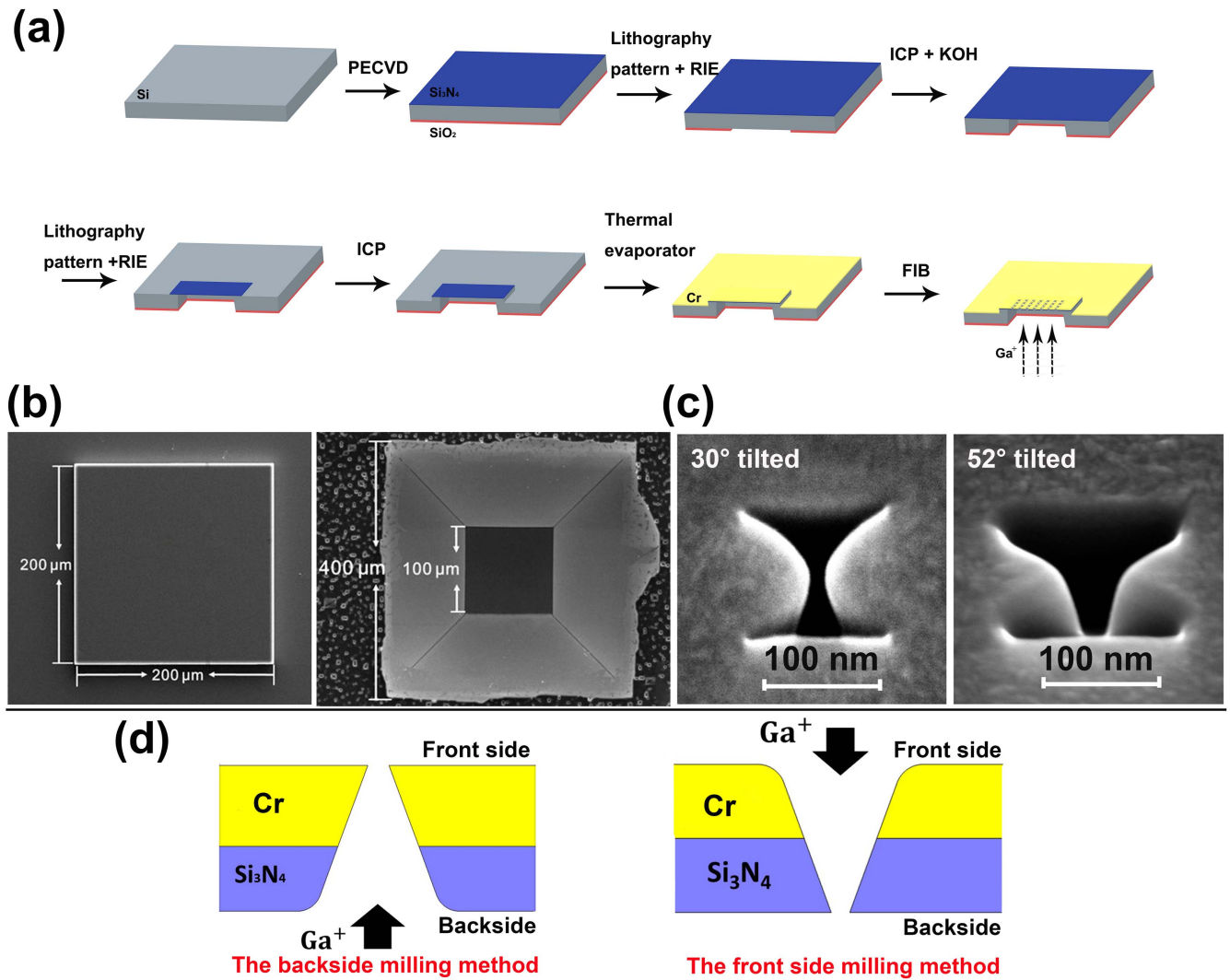
Figure 1. (a) Schematic drawing of the mask fabrication process. (b) SEM images of the island on the mask (left: the front side; right: the backside). (c) Tilted SEM images of bowtie apertures fabricated using the two milling methods (left: the backside milling method; right: the front-side milling method). (d) Schematic of the two aperture milling methods.

caused by the non-Gaussian tail of the ion beam [14, 15]. As a result, the lateral gap size is apparently enlarged; in previous works this has been found to be above 30 nm, something that seriously restricts its lithography resolution. In our former work [16], we have developed a new fabrication method named 'the backside milling method' to fabricate bowtie apertures with a sub-20 nm gap size. As such, near-field localization is notably improved, as testified by the scattering scanning near-field optical microscopy.

In this work, we apply the newly-developed backside milling method to fabricate bowtie apertures with an ultra-small gap for near-field lithography. The passive flexure stage is precisely designed to accurately control the contact condition between the mask and the substrate. As a consequence, the lithography resolution is improved to a record 16 nm (FWHM), which demonstrates great advantages over previously reported works on NSOL. The lithography results match well with the numerical calculations. This nanolithography scheme may further drive down nano-manufacturing resolution to a new era, which promises potential applications

in high-density data storage, biosensing, high-efficiency energy harvesting and so on [17–21].

2. Experiment and modeling

Figure 1(a) shows the fabrication process of the near-field lithography mask. A SiO_2 film (thickness: 2 μm) and a Si_3N_4 film (thickness: 300 nm) are deposited respectively on two sides of the Si wafer (thickness: 300 μm) using plasma enhanced chemical vapor deposition (PECVD) (Oxford System 100). Then three rectangles (400 μm $\times$ 400 μm) are patterned on the backside by optical lithography (SUSS MABA6), in which the SiO_2 film is removed by reactive ion etching (RIE) (Oxford NGP80). After that the Si wafer in the windows is etched out by inductively coupled plasma RIE (ICP-RIE) (Oxford ICP380) and KOH, leaving the Si_3N_4 film suspended. Then three islands (200 μm $\times$ 200 μm) are patterned at the front side aligned with the three windows using optical lithography. The Si_3N_4 film and a 20 μm thick Si layer
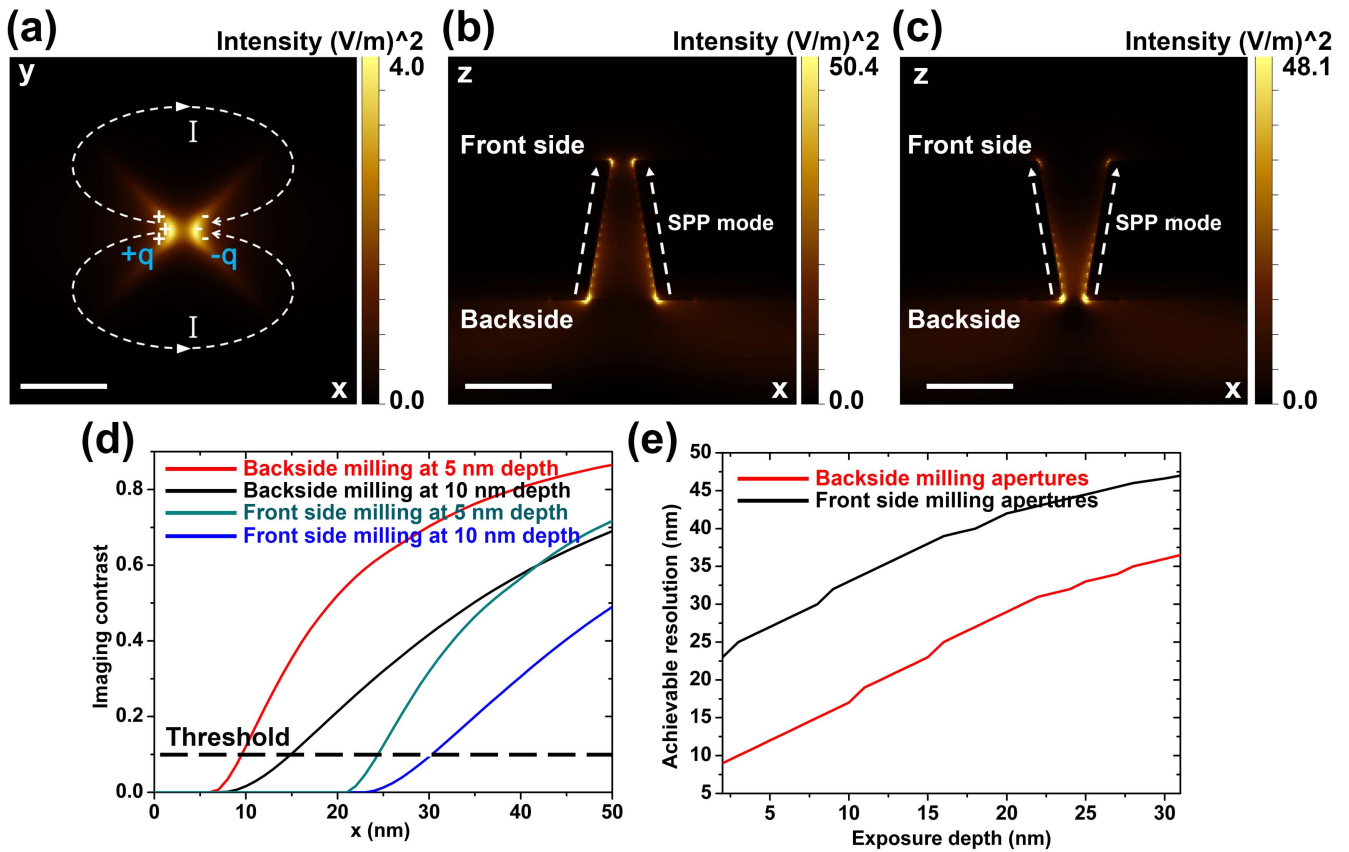
Figure 2. (a) FDTD simulation of the electric field intensity (background color), surface current (dotted line) and charges (signs) on the exit plane of the backside milling bowtie aperture made in the Cr film; scale bar: 50 nm. (b) and (c) Cross-sectional electric field intensity of the backside milling bowtie aperture (b) and the front-side milling bowtie aperture (c); scale bar: 50 nm. (d) Imaging contrast at different x coordinates for the two apertures at 5 nm and 10 nm exposure depth. (e) Achievable resolution as a function of exposure depth for the two apertures.

at the rest area is removed by RIE and ICP to form island structures, which help ensure contact between the mask and the photoresist. The SEM images of the island are depicted in figure 1(b). After that, a layer of chromium (80 nm) is deposited on the front side using a thermal evaporator with a rate of 0.2 A s^{-1}. Chromium is chosen because of its high film quality and good compatibility with the lubricant. Lastly, a FIB (FEI Helios 650, 30 kV and 7.7 pA) is used to mill bowtie apertures on the Si$_3$N$_4$ membrane from the backside of the mask through to the front side. We call this 'the backside milling method', which is different from 'the front-side milling method'. The schematic of the two fabrication methods is displayed in figure 1(d). Utilizing the backside milling method, the resultant non-vertical sidewall will not enlarge the gap size of the bowtie aperture on the metal surface. As a result, the lateral gap size can be consistently controlled below 15 nm, as shown in figure 1(c) (left). The outline dimension of the aperture is 120 nm × 130 nm. For comparison, a bowtie aperture fabricated using the front-side milling method has a gap size of 42 nm, as shown in figure 1(c) (right). Both the outline dimension and the lateral gap size on the metal surface are apparently enlarged.

Three-dimensional, finite-difference, time-domain (FDTD) simulations (Lumerical FDTD Solutions) are conducted to compare the near-field localization of the two apertures shown

in figure 1(c). Optical properties of Si$_3$N$_4$ and Cr are taken from Palik [22]. The refractive index of S1805 is 1.7433 at 355 nm. A plane wave polarized across the gap direction at the 355 nm wavelength is illuminated on the entrance plane of bowtie apertures. For the backside milling aperture, the electric near field is squeezed horizontally at the central gap in the xy-plane and vertically along the z-direction. In the xy-plane, as shown in figure 2(a), the surface current arises from one ridge, flows around the aperture and ends on the opposite ridge, depositing electric charges with opposite signs on the two ridges. The accumulated charges oscillate with the excitation electromagnetic field and act as an electric dipole. Due to the excitation of localized surface plasmon [23, 24], the electric field is enhanced and localized at the gap area and its confinement is decided by the gap size. Along the z-direction, the surface plasmon polariton (SPP) mode excited at the entrance plane is nanofocused to the narrower gap at the exit plane by the vertical taper [25–27], as shown in figure 2(b). Although the modal intensity is attenuated during transmission because of the propagation loss, the modal volume is compressed. Take the front-side milling aperture for comparison—relative to the backside milling aperture, its near-field confinement in the xy-plane is weakened due to its larger gap size and its SPP mode is diverged along the z-direction for its reversed taper, as shown in figure 2(c). As a result of the two factors, the electric field of
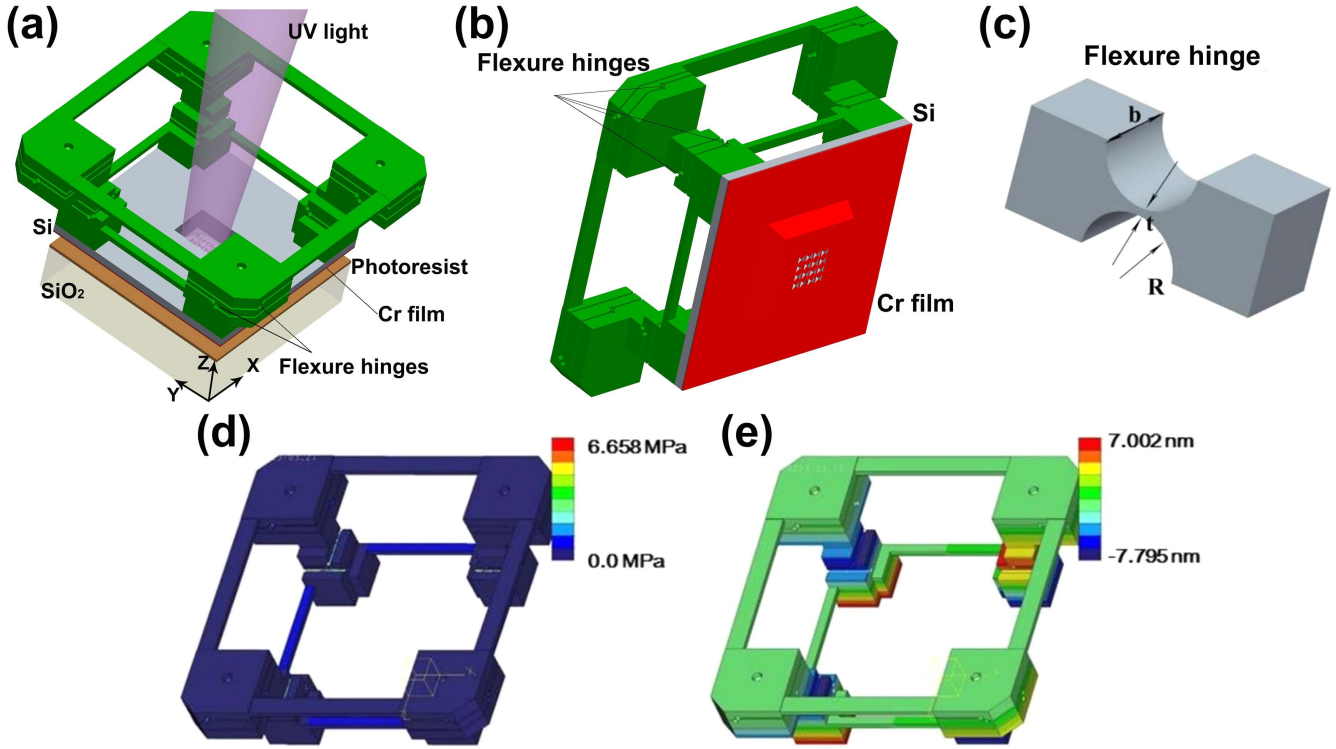
Figure 3. (a) Schematic drawing of the near-field optical lithography system. (b) Schematic drawing of the front side of the mask. (c) 3D model of a basic flexure hinge. (d) Stress distribution and (e) lateral deformation distribution of the passive stage using finite element analysis (FEA).

the backside milling aperture is much more confined than the front-side milling aperture.

Two factors decide the near-field lithography resolution: the transmitted field intensity distribution and the imaging contrast. Photoresist is sensitive to the total field intensity and a sufficient imaging contrast is required to expose patterns with good quality [28, 29]. The imaging contrast $M(z, r)$ is defined as:

$$M(z, r) = \frac{I_{\max}(z) - I(z, r)}{I_{\max}(z) + I(z, r)}, \tag{1}$$

where z is the distance from the exit plane and r is the radial coordinate. $I_{\max}(z)$ is the peak value of the light intensity in the plane and $I(z, r)$ is the intensity where the resolution needs to be evaluated. For the Shipley S1805 photoresist, an imaging contrast >0.1 is required to realize the corresponding resolution [30]. We can see from figure 2(d) that as the lithography depth decreases from 10 nm to 5 nm, the imaging contrast at a certain resolution apparently increases. By calculating the resolution value at a different depth where the imaging contrast equals 0.1, we can plot the achievable resolution as a function of the pattern depth for the two apertures, as shown in figure 2(e). Obviously, bowtie apertures fabricated using our method can achieve a higher resolution than bowtie apertures milled from the front side.

The schematic of the near-field lithography system is shown in figures 3(a) and (b). A linear polarized, diode-pumped, solid-state laser at 355 nm wavelength with 50 mW power is used as the exposure source. With a $5\times$ objective, the laser beam is loosely focused to a 1.5 mm $\times$ 1.5 mm spot

on the mask. The polarization of the laser is aligned across the gap of the bowtie aperture. The positive photoresist (Shipley S1805) used in our experiments is spun (4500 rpm) on a quartz substrate with a thickness of 450 nm. According to the data sheet of the photoresist, as the spin speed rises from 2000 rpm to 5000 rpm, the thickness of the photoresist decreases from 650 nm to 400 nm; it remains unchanged with a further increase of the spin speed above 5000 rpm. Our experiments agree well with the data sheet. After exposure, the photoresist is developed for 30 s. The substrate is mounted on a three-axis piezoelectric stage and the mask is held by a passive flexure stage [31]. The surface quality of the mask and the substrate is critical for good contact. By AFM characterization, the roughness of the photoresist is better than 2 nm and the flatness of the Cr film is better than 3 nm over the 200 μm $\times$ 200 μm island. An electrical switcher is used to accurately control the exposure dose. All the AFM measurements in our experiments are conducted in a tapping mode with a Bruker Dimension Icon. The AFM tip we use is the Arrow-NCR (Nanosensors) with a nominal tip radius of 10 nm which is able to resolve the lithography results in our work.

When bringing the substrate and the mask into contact, it is critical to minimize their relative lateral motion. The presence of sliding can cause wear and generate undesirable particles which will have a negative influence on lithography. During scanning, the interfacial forces, adhesion or friction, may cause unfavorable photoresist deformation, scanning hysteresis, or even mask breakage. To solve these problems, a
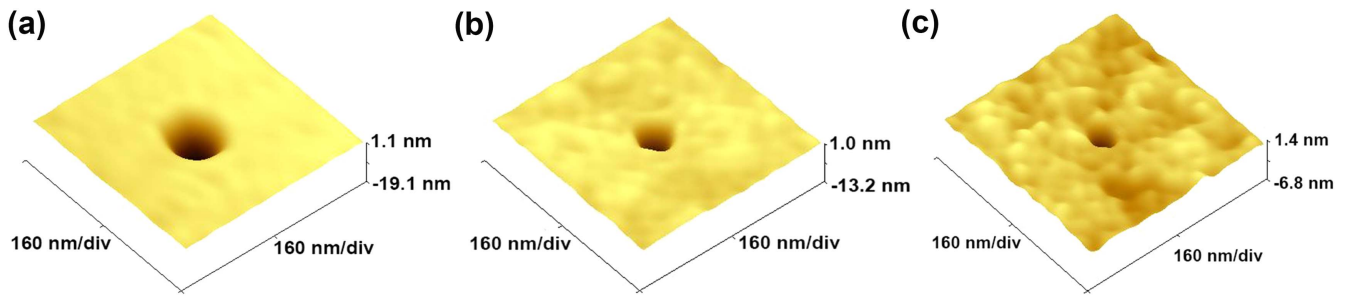
Figure 4. AFM images of lithography results using the same bowtie aperture with different exposure doses: (a) 1 s, (b) 0.5 s, (c) 0.2 s.
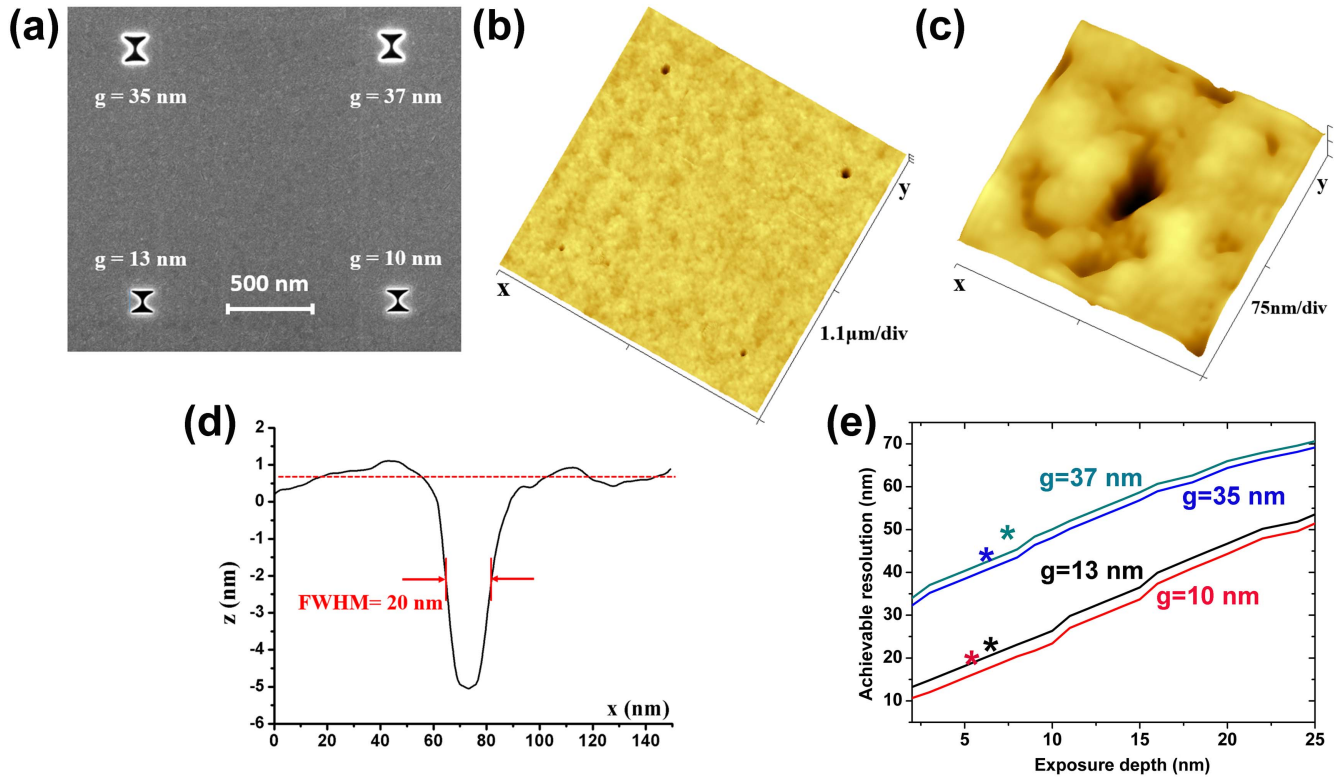

Figure 5. (a) SEM of the two kinds of bowtie apertures with their lateral gap size indicated for comparison. (b) AFM image of lithography results of the array. (c) Zoomed-in scan of the lower right hole. (d) Cross-section profile in the *x*-direction. (e) Achievable resolution as a function of patterning depth for the two kinds of bowtie apertures with different gap width *g*. The solid lines are obtained with the numerical analysis and the color asterisks are the experimental results.

passive flexure stage is applied in our lithography system [32]. A flexure hinge with a high off-axis stiffness is the fundamental unit of the stage, which incorporates a circular cutout on either side of the blank, as shown in figure 3(c). Its spring constant *k* can be calculated based on Paros and Weisbord's equation [33]. To maintain orientation motion between the mask and the substrate with a low load, two layers of hinges are designed with eight hinges in each layer. FEA is used to calculate the stress distribution and the lateral deformation distribution under a center load. A model mesh is generated as a free tetrahedral element type and is refined to improve the analytical accuracy. The top surface of the stage is fixed and a given vertical load 5 N is applied on the edge of the mask to mimic a small misalignment between the mask and the photoresist. The material of the hinges is aluminum alloy 7075-T6; its Young's modulus is 71.7 GPa and

Poisson's rate is 0.33. As shown in the stress distribution illustrated in figure 3(d), the stress is mainly concentrated at the circular hinges. Structural parameters of each hinge are optimized to maintain the lateral motion of the stage to be as small as 7.8 nm, as shown in figure 3(e). The lubricant Fomblin Z-dol which is compatible with Cr is also used in lithography to efficiently decrease the friction coefficient between the mask and the substrate by a factor of three. This 2 nm-thick lubricant layer has little influence on the near-field distribution, thus it is ignored in the numerical simulations.

3. Results and discussion

Precise control of the exposure dose is critical to achieve high lithography resolution; this is achieved through exposure time
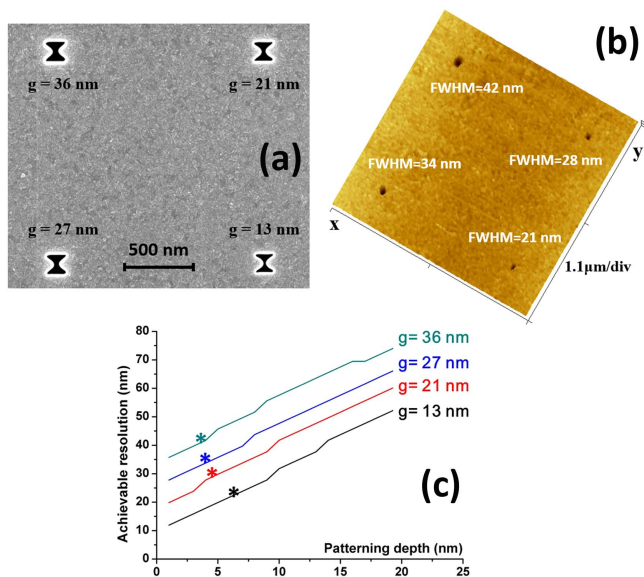
Figure 6. (a) SEM of four bowtie apertures with different scan passes and gap sizes. (b) AFM image of lithography results of the aperture array with the FWHM of each hole indicated. (c) Achievable resolution as a function of patterning depth for bowtie apertures with different gap widths *g*. The solid lines are obtained with the numerical analysis and the color asterisks are the experimental results.

control in our experiments. Lithography results using the same bowtie aperture with different exposure times (1 s, 0.5 s and 0.2 s) are shown in figure 4. Longer exposure time leads to larger and deeper holes with worse resolution, but too short an exposure time (<0.2 s in this case) will result in no lithography results. Thus, a threshold dose needs to be calibrated and used to achieve the best resolution.

In order to compare the lithography performance of the bowtie apertures fabricated using the two different milling methods, an array composed of two front-side milling bowtie apertures (upper) and two backside milling bowtie apertures (lower) is fabricated and used for the lithography, as shown in figure 5(a). By properly controlling the exposure dose, lithography at 0.2 s gives the best resolution. It can be seen from figure 5(b) that the lithography resolution is apparently improved by using the backside milled bowtie apertures for its better near-field confinement, which agrees well with the numerical calculations, as shown in figure 5(e). A zoomed-in scan of the lower right hole gives a resolution of 20 nm (FWHM) in the *x*-direction, as shown in figures 5(c) and (d). Deconvolution of the measured hole topography with the geometric model of the AFM tip gives a FWHM value of 24 nm. The FWHM in the *y*-direction is 27 nm because of the relatively larger longitudinal gap size, which can be reduced by optimization of the ion scan path [34]. As a comparison, the zoomed-in scan of the upper left hole gives a FWHM of 48 nm.

The gap size of the bowtie aperture decides its near-field localization. To evaluate the influence of the gap size on the lithography performance, we fabricated four bowtie apertures with different gap sizes using the backside milling method by simply changing the ion scan passes while fixing the ion

dwell time on a single pixel (figure 6(a)). As shown in figure 6(b), the lithography results demonstrate that a larger gap size leads to worse lithography resolution. In figure 6(c), we plot the achievable resolution of bowtie apertures with different gap sizes as a function of patterning depth using the numerical method described above. The experimental results are also presented in the figure, which agree well with the analytical results. As a conclusion, the bowtie aperture with a smaller gap size can achieve a higher lithography resolution.

With the assistance of the flexure stage and lubricant, the substrate can be scanned below the lithography mask while maintaining good contact. Otherwise, the interfacial forces, adhesion or friction may cause an unfavorable photoresist deformation, scanning hysteresis, or even mask break [35]. The exposure dose is adjusted by the scanning speed. A slower scan results in a deeper and broader groove. Considering that the lithography line is formed by overlapping between two adjacent lithography holes, a higher resolution can be achieved by scanning lithography compared to static lithography [36]. During scanning, the apertures will not be rotated with different scan directions. As shown in figure 5(c), the dimension of the exposure hole is 20 nm in the *x*-direction and 27 nm in the *y*-direction. Such a deviation results in different lithography linewidths along different scan directions, which, however, is not apparent, as shown in figure 7(a). Rotating apertures will cause slide contact between the mask and the photoresist, weaken the function of the lubricant system and make the orientation of the apertures misalign with the polarization of the exposure laser. Figure 7(a) shows a pattern 'USTC' produced using our NSOL system. AFM scanning gives a record 12 nm lithography resolution (FWHM) at a scan speed of 0.2 μm s^{-1}, as shown in figures 7(b) and (c). Deconvolution of the measured trench profile with the geometric model of the AFM tip (Arrow-NCR from Nanosensors with a nominal tip radius of 10 nm) gives a FWHM value of 16 nm.

Similar to FIB or E-beam lithography, NSOL fabrication speed can change significantly depending on the fabrication resolution and exposure power. Overall its fabrication speed is comparable to FIB or E-beam lithography. However, compared with FIB or E-beam lithography, NSOL is much cheaper and more convenient. The total cost of the setup is only ~5% of the FIB or E-beam cost. Furthermore, it does not require high vacuum techniques and conductive substrates.

The optical near field of the bowtie aperture is evanescent and decays rapidly with increased distance from the aperture; the exposure depth is therefore limited in our work, which is a common problem in NSOL [10, 35, 37–39]. If the Shipley S1805 photoresist is diluted with the related diluent and then spin-coated, the minimum thickness it can achieve is 19 nm, which is still much larger than the exposure depth of our near-field lithography. An increasing exposure dose can deepen the lithography pattern at the expense of seriously worsening the resolution. Adding a reflective slab can be an efficient approach to increasing the exposure depth while maintaining a high resolution, but it will make the lithography process much more complicated [40]. The shallow exposure depth in the photoresist can impede the following pattern transfer
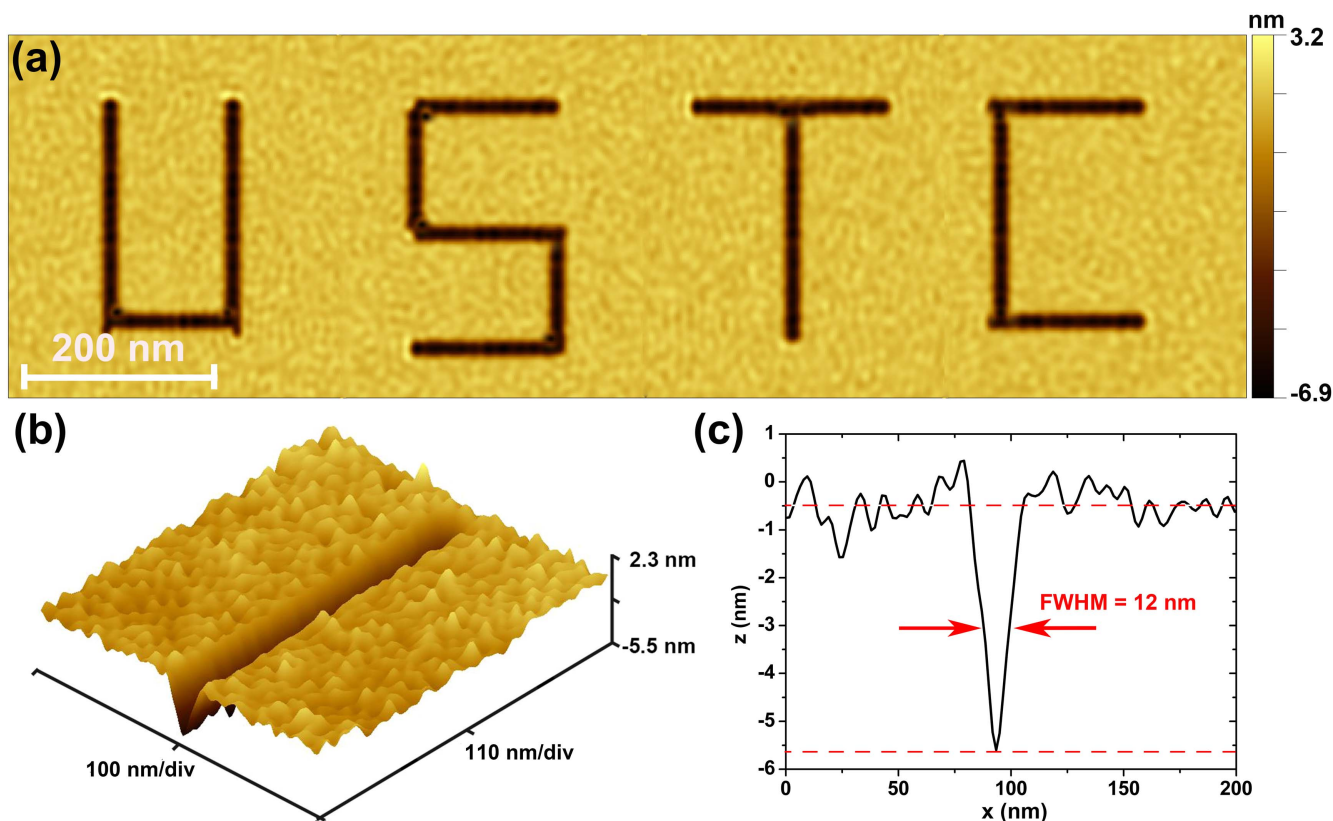
Figure 7. (a) AFM image of a pattern produced by NSOL. (b) Zoomed-in image of the line at the lower part of the character 'T'. (c) Cross-sectional profile of the line.

process, which is still under investigation by a number of groups around the world.

4. Conclusions

In conclusion, we have presented NSOL using bowtie apertures with a sub-15 nm gap, which are fabricated using the backside milling method. Combined with the passive flexure stage for contact control, we have realized a record 16 nm-resolution lithography. By further decreasing the gap size of the bowtie aperture via combining the proximity milling technique and optimizing the contact condition, the near-field lithography resolution promises further refinement in the future. This low-cost photolithography scheme can find its potential applications in data storage, energy harvesting, high-speed computation and so on.

References

[1] Xie Z, Yu W, Wang T, Zhang H, Fu Y, Hua L, Li F, Lu Z and Qiang S 2011 Plasmonic nanolithography: a review *Plasmonics* **6** 565–80
[2] Park M and Adamson D H 1997 Block copolymer lithography: periodic arrays of ∼1011 holes in 1 square centimeter *Science* **276** 1401–4
[3] Valsesia A, Meziani T, Bretagnol F, Colpo P, Ceccone G and Rossi F O 2007 Plasma assisted production of chemical nano-patterns by nano-sphere lithography: Application to bio-interfaces *J. Phys. D: Appl. Phys.* **40** 2341–7
[4] Xiaowei G, Jinglei D, Yongkang G and Jun Y 2006 Large-area surface-plasmon polariton interference lithography *Opt. Lett.* **31** 2613–5
[5] Guo L J 2007 Nanoimprint lithography: methods and material requirements *Adv. Mater.* **19** 495–513
[6] Liang X, Jung Y-S, Wu S, Ismach A, Olynick D L, Cabrini S and Bokor J 2010 Formation of bandgap and subbands in graphene nanomeshes with sub-10 nm ribbon width fabricated via nanoimprint lithography *Nano Lett.* **10** 2454–60

[7] Wang L, Uppuluri S M, Jin E X and Xu X F 2006 Nanolithography using high transmission nanoscale bowtie apertures *Nano Lett.* **6** 361–4

[8] Uppuluri S M V, Kinzel E C, Li Y and Xu X F 2010 Parallel optical nanolithography using nanoscale bowtie aperture array *Opt. Express* **18** 7369–75

[9] Wang L, Jin E X, Uppuluri S M and Xu X F 2006 Contact optical nanolithography using nanoscale C-shaped apertures *Opt. Express* **14** 9902–8

[10] Kim S, Jung H, Kim Y, Jang J and Hahn J W 2012 Resolution limit in plasmonic lithography for practical applications beyond 2x-nm half pitch *Adv. Mater.* **24** 337–44

[11] Jin E X and Xu X 2006 Enhanced optical near field from a bowtie aperture *Appl. Phys. Lett.* **88** 153110

[12] Jin E X and Xu X 2005 Obtaining super resolution light spot using surface plasmon assisted sharp ridge nanoaperture *Appl. Phys. Lett.* **86** 111106

[13] Ali M Y, Hung W and Fu Y Q 2010 A review of focused ion beam sputtering *Int. J. Precis Eng. Man* **11** 157–70

[14] Frey L, Lehrer C and Ryssel H 2003 Nanoscale effects in focused ion beam processing *Appl. Phys. A* **76** 1017–23

[15] Ishitani T 2004 Improvements in performance of focused ion beam cross-sectioning: aspects of ion-sample interaction *J. Electron Microsc.* **53** 443–9

[16] Chen Y, Chen J, Xu X and Chu J 2015 Fabrication of bowtie aperture antennas for producing sub-20 nm optical spots *Opt. Express* **23** 9093–9

[17] Stipe B C *et al* 2010 Magnetic recording at 1.5 Pb m^{-2} using an integrated plasmonic antenna *Nat. Photonics* **4** 484–8

[18] Anker J N, W Paige H, Olga L, Shah N C, Jing Z and Van Duyne R P 2008 Biosensing with plasmonic nanosensors *Nat. Mater.* **7** 442–53

[19] Linic S, Christopher P and Ingram D B 2011 Plasmonic-metal nanostructures for efficient conversion of solar to chemical energy *Nat. Mater.* **10** 911–21

[20] Mubeen S, Hernandez-Sosa G, Moses D, Lee J and Moskovits M 2011 Plasmonic photosensitization of a wide band gap semiconductor: converting plasmons to charge carriers *Nano Lett.* **11** 5548–52

[21] Chen Y, Chu J R and Xu X F 2016 Plasmonic multibowtie aperture antenna with Fano resonance for nanoscale spectral sorting *ACS Photonics* **3** 1689–97

[22] Palik E D 1985 Handbook of optical constants of solids *Academic Press Handbook* **33** 189

[23] Jin E X and Xu X 2006 Plasmonic effects in near-field optical transmission enhancement through a single bowtie-shaped aperture *Appl. Phys. B* **84** 3–9

[24] Garcia-Vidal F J, Moreno E, Porto J A and Martin-Moreno L 2005 Transmission of light through a single rectangular hole *Phys. Rev. Lett.* **95** 103901

[25] Kim M K, Sim H, Yoon S J, Gong S H, Ahn C W, Cho Y H and Lee Y H 2015 Squeezing photons into a point-like space *Nano Lett.* **15** 4102–7

[26] Sondergaard T, Bozhevolnyi S I, Beermann J, Novikov S M, Devaux E and Ebbesen T W 2010 Resonant plasmon nanofocusing by closed tapered gaps *Nano Lett.* **10** 291–5

[27] Sondergaard T, Bozhevolnyi S I, Novikov S M, Beermann J, Devaux E and Ebbesen T W 2010 Extraordinary optical transmission enhanced by nanofocusing *Nano Lett.* **10** 3123–8

[28] Madou M J 2011 *Fundamentals of Microfabrication* (Taylor and Francis)

[29] Wang L and Xu X 2008 Numerical study of optical nanolithography using nanoscale bow-tie-shaped nano-apertures *J. Microsc* **229** 483–9

[30] Alkaisi M, Blaikie R and McNab S 2000 70 nm Features on 140 nm period using evanescent near field optical lithography *Microelectron. Eng.* **53** 237–40

[31] Choi B J, Sreenivasan S V, Johnson S, Colburn M and Wilson C G 2001 Design of orientation stages for step and flash imprint lithography *Precision Eng.* **25** 192–9

[32] Ouyang P 2011 A spatial hybrid motion compliant mechanism: design and optimization *Mechatronics* **21** 479–89

[33] Paros J M 1965 How to design flexure hinges *Mach. Des.* **37** 151–6

[34] Kim H-B 2012 Multiple surface driving method for the accurate sculpting of predefined arbitrary surfaces in the micro/nano regime *Microelectron. Eng.* **91** 14–8

[35] Wen X, Datta A, Traverso L M, Pan L, Xu X and Moon E E 2015 High throughput optical lithography by scanning a massive array of bowtie aperture antennas at near-field *Sci. Rep.* **5** 16192

[36] Xu M and Arce G R 2009 Pixel-based simultaneous source and mask optimization for resolution enhancement in optical lithography *Opt. Express* **17** 5783–93

[37] Pan L, Park Y, Xiong Y, Ulin-Avila E, Wang Y, Zeng L, Xiong S, Rho J, Sun C and Bogy D B 2011 Maskless plasmonic lithography at 22 nm resolution *Sci. Rep.* **1** 00175

[38] Wang Y, Srituravanich W, Sun C and Zhang X 2008 Plasmonic nearfield scanning probe with high transmission *Nano Lett.* **8** 3041–5

[39] Kim Y, Kim S, Jung H, Lee E and Hahn J W 2009 Plasmonic nano lithography with a high scan speed contact probe *Opt. Express* **17** 19476–85

[40] Luo J, Zeng B, Wang C, Gao P, Liu K, Pu M, Jin J, Zhao Z, Li X and Yu H 2015 Fabrication of anisotropically arrayed nano-slots metasurfaces using reflective plasmonic lithography *Nanoscale* **7** 18805–12